Experimental investigation of the behavior of UHPCFST under repeated eccentric compression

Chunlei Yu[a], Min Yu[a*], Lihua Xu[a], Sumei Liu[a], Zewen Sun[a], Jianqiao Ye[b]
[a] School of Civil Engineering, Wuhan University, Wuhan 430072, China
[b] School of Engineering, Lancaster University, Lancaster LA1 4YR. UK

Abstract: This paper investigates the mechanical behavior of ultra-high-performance concrete-filled steel tubes (UHPCFST) under repeated eccentric compression. A total of 30 UHPCFST specimens are designed, fabricated, and tested. The design variables include steel tube thickness, UHPC type, loading eccentricity and load pattern. Failure modes, force-axial shortening curves, section strain distributions, lateral deflection distributions, bearing capacity and stiffness are studied. Three failure modes, *i.e.*, steel tube bulge, compressive crush and tensile crack of the UHPC infill are observed. Specimens with larger loading eccentricity and thinner steel tube are more likely to exhibit all the three modes. Subjected to eccentric loading, the compressive strength and stiffness of the UHPCFST increase significantly with the increase of steel tube thickness and UHPC strength. In the case of repeated loading, stiffness degradation is observed. Existing formulas for the N-M curve and the eccentric compressive capacity are evaluated against the test results. A formula for eccentric compressive stiffness is derived based on the parabolic function assumption. Additionally, an empirical model is introduced to describe the force-axial shortening relationship of the UHPCFST under repeated eccentric compression, which may be applied in practical design and analysis.

Keywords: UHPCFST, mechanical behavior, repeat eccentric compression

1. Introduction

Due to its advantages such as affordability, malleability, and high compressive strength, concrete has become one of the most widely used construction materials over centuries [1]. Numerous studies have shown that the mechanical properties of concrete significantly improve when subjected to tri-compression [2–4]. Concrete-Filled Steel Tubes (CFSTs) exploit this property and have gained significant attention in the field of structural engineering[5–7]. CFST technology has found practical applications in. i.e., civil constructions, including high-rise buildings[8], bridges[9], and cooling towers[10]. In pursuit of higher mechanical properties, a promising cement-based material known as Ultra-High-Performance Concrete (UHPC) [11–13] emerged and has the potential to replace traditional concrete. Filling steel tube with UHPC leads to the a high performance composite form known as Ultra-High-Performance Concrete-Filled Steel Tube (UHPCFST) [14–17]. This high-performance and innovative composite component is gaining increasing attention and is being recognized as a significant potential structural form for the future of construction and engineering.

In the recent decades, a structure form, diagrid structure, draws most attentions in the area of civil engineering[18–20], seen in Fig.1. Compared to the common frame structure with horizontal beams and vertical columns, a diagrid structure removes almost all horizontal components and uses diagrid columns to provide lateral stiffness and axial stiffness simultaneously, providing required lateral stiffness for earthquake resistance design. During an earthquake, columns in diagrid structures will undergo axial or eccentric loading cycles. CFST exhibit superior mechanical behavior under axial or eccentric loading, which can explains why they have been widely used in diagrid structures[21,22], such as the Guangzhou West Tower and the Guangzhou Television Tower. Consequently, the axial and eccentric compression responses of CFST remain a hot topic of research. Han[7] conducted numerous eccentric loading tests on CFST and developed an N-M curve to predict eccentric load-bearing capacity. Inspired by traditional CFST, Carbon-FRP[23], inner spiral stirrup[24], different section type (L-shaped[25] and T-shaped[26]) and concrete-encased[27] enhancement CFST have also been studied under eccentric compression. Despite these advancements, research on UHPCFST subjected to repeated eccentric compression is still lacking, which is important to evaluate its seismic performance. Recent studies have shown promising results in the axial[28,29] and flexural[30] performance of UHPCFST, particularly in enhancing load-bearing capacity and ductility. However, the understanding of its behavior under repeated eccentric loading conditions remains limited. It's urgent to conduct studies to address this knowledge gap.

a). GuangZhou West Tower **b).** Cooling tower of power plant

Fig.1. Engineering applications of diagrid structure

In section 2, thirty UHPCFSTs are subjected to both monotonic and repeated eccentric compression tests to examine their mechanical properties. the experimental program, including specimens design, materials tests, test set-up and loading pattern, is introduced. In section 3, the failure modes, force-axial shortening curve, section strain distribution, lateral deflection distribution and presented, based on those test results, bearing capacity, loading stiffness and stiffness degradation are systematically analyzed. In section 4, an empirical model is proposed to describe the relationship between force and axial shortening of UHPCFST under repeated eccentric compression. In the empirical model, eccentric bearing capacity and stiffness are discussed in detail. Existed formulas for predicting eccentric compressive bearing capacity of CFST are assessed. A formula to estimate the initial stiffness under eccentric compression is developed, and a formula for stiffness degradation is proposed, which enables the calculation of unloading and reloading stiffness.

2. Experimental program

2.1. Specimen design

Thirty UHPCFST specimens are tested to investigate the mechanical behavior of UHPCFST under repeated eccentric compression. Three types of UHPC, each with a different volume fraction of coarse aggregate, are used along with three different steel tubes to fabricate the specimens. The specimens are divided into two groups of fifteen: one for monotonic eccentric compression tests and the other for repeated eccentric compression tests. The monotonic loading specimens are designed for comparative analysis in terms of mechanical responses such as the skeleton curve and damage evolution with repeated loading specimens. The design details of all the thirty specimens are provided in Table.1. The steel tubes have a diameter of 168 mm, and the height of each specimen is three times its diameter to ensure stability. Steel thicknesses of 6 mm, 8 mm, and 10 mm are used to assess the impact of steel confinement. The volume fractions of coarse aggregate are 0%, 15%, and 30%, respectively. Additionally, eccentricities of 10 mm, 30 mm, and 50 mm are chosen to study the effect of the eccentricity of the imposed compression load.

Table.1 Specimen design.

Label	t	e	f_y	E_y	V_{ca}	f_{cu}	f_{ck}	α	ξ	Loading

	(mm)	(mm)	(MPa)	(GPa)	(%)	(MPa)	(MPa)			Type
D168T6CA15E10-M	6	10	450	209	15	134	114	0.160	0.631	Monotonic
D168T6CA15E30-M	6	30	450	209	15	134	114	0.160	0.631	Monotonic
D168T6CA15E50-M	6	50	450	209	15	134	114	0.160	0.631	Monotonic
D168T8CA15E10-M	8	10	374	210	15	134	114	0.222	0.727	Monotonic
D168T8CA15E30-M	8	30	374	210	15	134	114	0.222	0.727	Monotonic
D168T8CA15E50-M	8	50	374	210	15	134	114	0.222	0.727	Monotonic
D168T10CA15E10-M	10	10	401	208	15	134	114	0.289	1.015	Monotonic
D168T10CA15E30-M	10	30	401	208	15	134	114	0.289	1.015	Monotonic
D168T10CA15E50-M	10	50	401	208	15	134	114	0.289	1.015	Monotonic
D168T6CA00E10-M	6	10	450	209	0	125	101	0.160	0.712	Monotonic
D168T6CA00E30-M	6	30	450	209	0	125	101	0.160	0.712	Monotonic
D168T6CA00E50-M	6	50	450	209	0	125	101	0.160	0.712	Monotonic
D168T6CA30E10-M	6	10	450	209	30	142	129	0.160	0.557	Monotonic
D168T6CA30E30-M	6	30	450	209	30	142	129	0.160	0.557	Monotonic
D168T6CA30E50-M	6	50	450	209	30	142	129	0.160	0.557	Monotonic
D168T6CA15E10-R	6	10	450	209	15	134	114	0.160	0.631	Repeated
D168T6CA15E30-R	6	30	450	209	15	134	114	0.160	0.631	Repeated
D168T6CA15E50-R	6	50	450	209	15	134	114	0.160	0.631	Repeated
D168T8CA15E10-R	8	10	374	210	15	134	114	0.222	0.727	Repeated
D168T8CA15E30-R	8	30	374	210	15	134	114	0.222	0.727	Repeated
D168T8CA15E50-R	8	50	374	210	15	134	114	0.222	0.727	Repeated
D168T10CA15E10-R	10	10	401	208	15	134	114	0.289	1.015	Repeated
D168T10CA15E30-R	10	30	401	208	15	134	114	0.289	1.015	Repeated
D168T10CA15E50-R	10	50	401	208	15	134	114	0.289	1.015	Repeated
D168T6CA00E10-R	6	10	450	209	0	125	101	0.160	0.712	Repeated
D168T6CA00E30-R	6	30	450	209	0	125	101	0.160	0.712	Repeated
D168T6CA00E50-R	6	50	450	209	0	125	101	0.160	0.712	Repeated
D168T6CA30E10-R	6	10	450	209	30	142	129	0.160	0.557	Repeated
D168T6CA30E30-R	6	30	450	209	30	142	129	0.160	0.557	Repeated
D168T6CA30E50-R	6	50	450	209	30	142	129	0.160	0.557	Repeated

In Table.1, t and e denote, respectively, thickness and load eccentricity; V_{ca} is coarse aggregate volume fraction of concrete; f_{cu} is cubic compressive strength of UHPC; f_{ck} is cylinder compressive strength of UHPC; f_y is yield strength of steel; α is steel ratio, for circle section, $\alpha=4t/d$; ξ is confinement factor[7]. The specimens to be tested are labeled with D*i*T*i*CA*jk*E*pq*-*L*, where D*i* denotes diameters of *i*mm, Ti denotes thickness of *i*mm, CA*jk* denotes coarse aggregate volume fraction of *jk*% , E*pq* denotes impost load eccentricity of *pq* mm and *L* takes M for monotonic loading and R for repeated loading, respectively.

2.2. Materials tests

2.2.1. Steel tube

Steel coupons were fabricated from the steel tube according to the Chinese code GB/T 228.1:2010[31]. The tensile tests were executed using a 60T tension-compression quasi-dynamic testing machine located in the Structural Engineering laboratory of Wuhan University. The force sensor of the machine is used to record the applied force, and an extensometer is mounted on the test sample to record the tensile strain. The tests are operated under displacement loading control at a speed of 0.5 mm/min. The primary failure mode is consistently characterized by fractures at the center of the specimens. Stress-strain curves show yield plateaus, as depicted in Fig.2. Table.2 presents the yield strength, ultimate strength, elastic modulus, and Poisson’s ratio of the steel coupon samples.

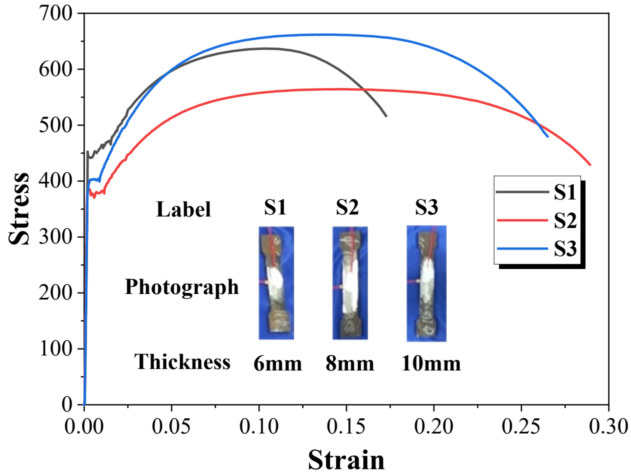

Fig.2. Strain-stress curve of steel tube.

Table.2 Properties of steel tube

No	Sample Label	Seamless steel tube diameter(mm)	Thickness (mm)	Yield stress (MPa)	Ultimate stress (MPa)	Elastic module (GPa)	Poisson's ratio
1	S1	168	6	450	636	209	0.30
2	S2	168	8	374	564	210	0.31
3	S3	168	10	401	661	208	0.28

2.2.2. UHPC

Three ultra-high-performance concrete (UHPC) mixtures are examined to study the impact of coarse aggregate volume fraction on the UHPCFST eccentric compressive behavior. A detailed description of these mixtures is provided in Table.3. The concrete binder comprises P.O.52.5 cement, silica fume with 95% silicon content, and fly ash. Polypropylene fibers with a diameter of 18-48 μm and straight copper-coated steel fibers measuring 13 mm in length and 0.2 mm in diameter are added to the mixture. Highly efficient polycarboxylate superplasticizer powders are utilized to augment the fluidity of the fresh mixture. The UHPC incorporates quartz sand, with a particle size of 69-178 μm as the fine aggregate, and basalt, with a size range of 5-10 mm as the coarse aggregate. Based on the recommendations from previous research [29,30], three coarse aggregate volume fractions are selected: 0%, 15%, and 30% (referred to as CA00, CA15, and CA30, respectively). These fractions are chosen to balance the strength and workability of the UHPC.

Table.3 Mixture of UHPC

Mixture (kg/m^3)	Cement	Silica fume	Fly ash	Water	Quartz sand	Coarse Aggregate	Super plasticizer	Steel fiber	Polypropylene fiber
UHPC-CA00	857	107	107	182	1179	-	11.8	157(2%)	1.9(0.2%)
UHPC-CA15	725	91	91	154	998	375(15%)	10	157(2%)	1.9(0.2%)
UHPC-CA30	594	74	74	126	817	750(30%)	8.2	157(2%)	1.9(0.2%)

According to the Chinese Code T/CCPA 35—2022[32], cubic samples (100mm x 100mm x 100mm) are fabricated to measure the cubic compressive strength. Additionally, cylinder samples measuring 100mm in diameter and 200mm in height are made to measure the cylinder compressive strength and elastic modulus. The measured mechanical properties are presented in Table.4

Table.4 Mechanical Properties of UHPC

UHPC	Cubic compressive strength (MPa)	Cylinder compressive strength (MPa)	Elastic module (GPa)

UHPC-CA00	126	101	47
UHPC-CA15	135	114	48
UHPC-CA30	143	129	51

2.3. Test set-up and load patterns

Eccentric compression tests on the UHPCFST are conducted on a shear-compression testing machine with a maximum capacity of 30,000kN in the Structural Engineering laboratory at Wuhan University . To accommodate rotational degrees of freedom at both ends of the specimens, two cylinder-hinges are designed and positioned between the loading plates of the test machine and the endplates of the specimen. These hinges are aligned vertically during the test setup. The eccentricity of the load is measured from the central vertical axis of the specimen to the center of the cylindrical hinges. Axial and lateral deformations of the specimens are measured using Linear Variable Differential Transformers (LVDTs). The axial force and axial shortening of the specimen are recorded by the loading machine. Five LVDTs are strategically placed laterally at quarter-height intervals to assess the distribution of lateral deformation. In addition to displacement measurement, five pairs of gauges are attached to the surface of the steel tube of the specimen to monitor the real-time distribution of the horizontal and vertical strain along the mid-height section. The setup of the test is illustrated in Fig.3.

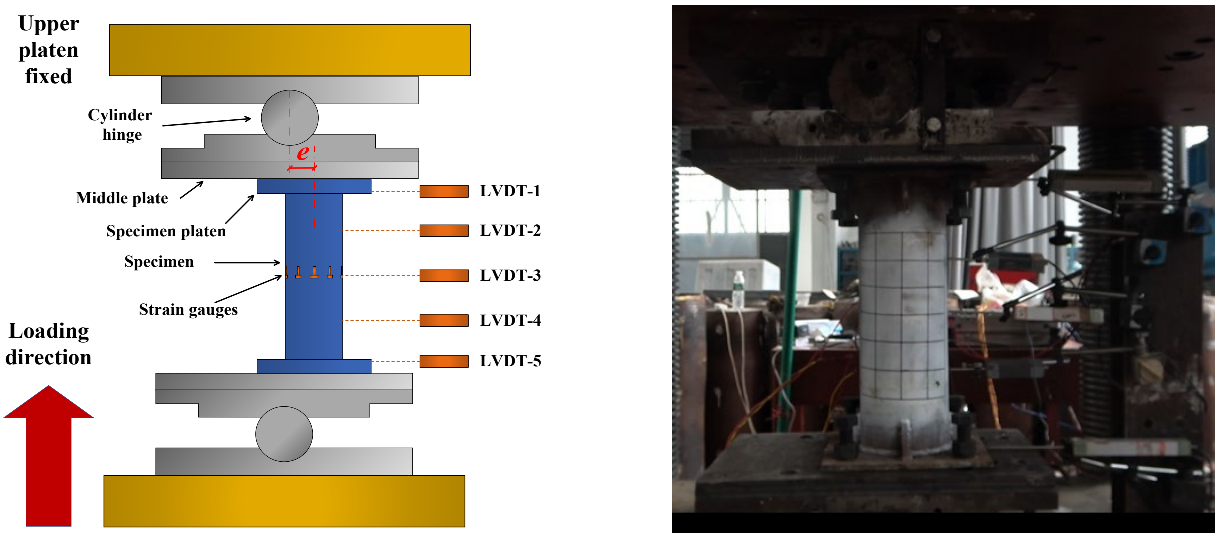

c). Schematic diagram **d).** Photograph

Fig.3. Test set-up

The experiment considers two different loading patterns: monotonic eccentric compression and repeated eccentric compression. Displacement-controlled loading is conducted with varying loading rates and increments, as illustrated in Fig.4. In the case of monotonic eccentric compression, a constant loading rate of 1 mm/min is applied until the displacement reaches one-tenth of the specimen height. For the repeated eccentric compression tests, a loading rate of 1 mm/min and a displacement increment of 0.3% of the specimen height is applied until specimen yields. Subsequently, the loading rate is increased to 2 mm/min, and the displacement increment per loading cycle is increased to 1% of the specimen height until the displacement reached one-tenth of the specimen height.

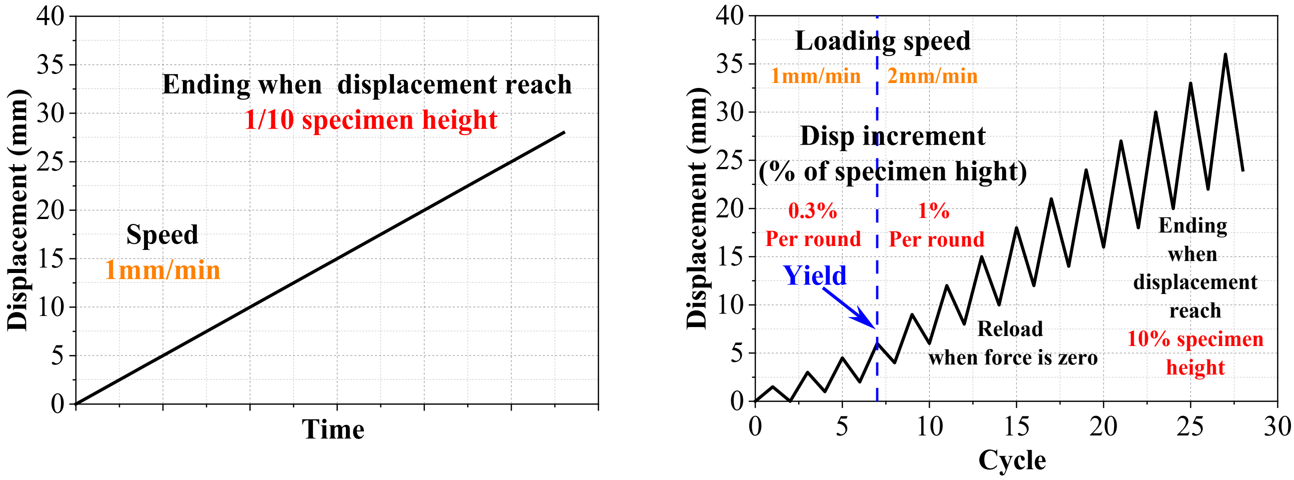

a). Monotonic eccentric compression **b).** Repeated eccentric compression

Fig.4. Displacement controlled Load patterns

3. Test results and analysis

3.1. Test results

3.1.1. Failure modes

After the eccentric compressive tests, the steel tubes are removed from the specimens. Fig.5 displays photos of specimens illustrating the respective failure modes of the UHPC infill. The typical failure mode comprises three features: bulging of the steel tube, compressive crushing and tensile cracking of the UHPC infill. The combination of these features defines the failure modes of the UHPCFST, which are dependent on the design variables. The bulging of the steel tube is more likely to occur in specimens with smaller eccentricity, thinner tube thicknesses and higher UHPC coarse aggregate volume fraction. Compressive crushing of the UHPC infill is observed in all test specimens. Horizontal tensile cracking of the UHPC infill does not occur when the eccentricity is small, such as 10 mm in this study. Specimens with a larger eccentricity, thinner steel tube thicknesses and higher UHPC coarse aggregate volume fraction tend to exhibit more severe compressive crushing and tensile cracking in the UHPC infill.

D168T10CA15E10 D168T10CA15E30 D168T10CA15E50

a). Effect of eccentricity

D168T6CA00E10 D168T6CA15E10 D168T6CA30E10

b). Effect of coarse aggregate volume fraction

D168T6CA15E50 D168T6CA15E50 D168T10CA15E50

c). Effect of steel tube thickness

Fig.5. Failure modes of UHPCFSTs under eccentric compression

3.1.2. Force versus axial shortening curve

The compressive force (N) applied to the specimens is plotted against the axial shortening (Δ) in Fig.6. The N-Δ curves of all the tested UHPCFST specimens exhibit similar characteristics. In the case of a specimen under monotonic compression, the curve initially shows an linear phase until the steel tube yields. After linear phase, an elastic-plastic phase follows, and this phase end up with the curve reaches its peak point. Finally, a descending phase occurs where the compressive force decreases as the strain increases. In the case of a specimen under repeated compression, an additional unload and reload phase is added, the N-Δ nearly remains linear in this phase.

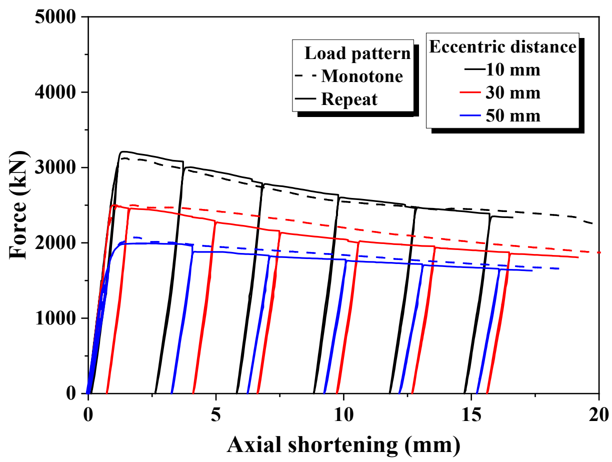

a). D168T6CA00

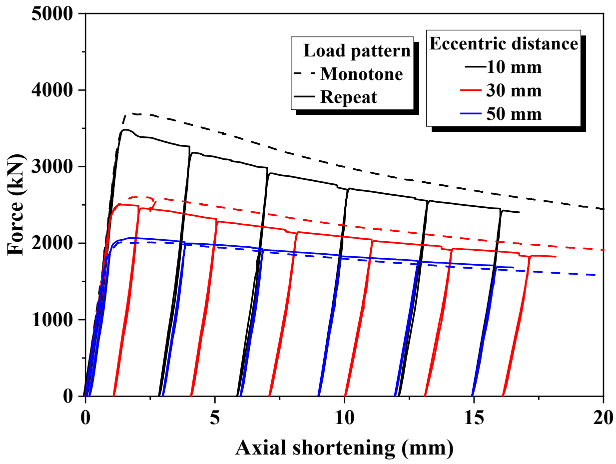

b). D168T6CA15

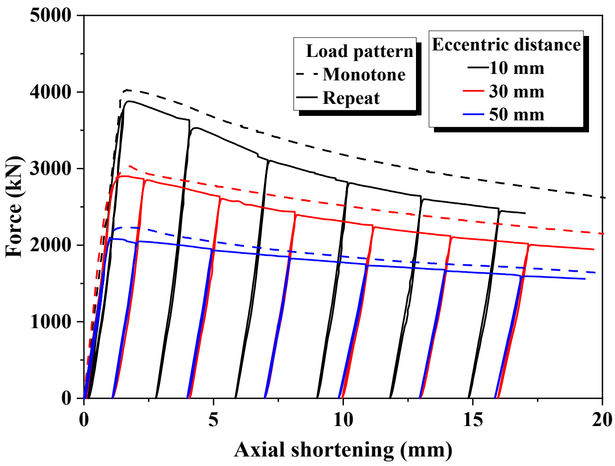

c). D168T6CA30

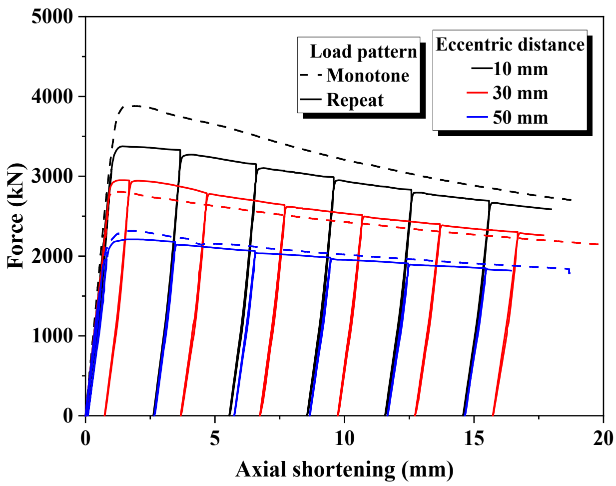

d). D168T8CA15

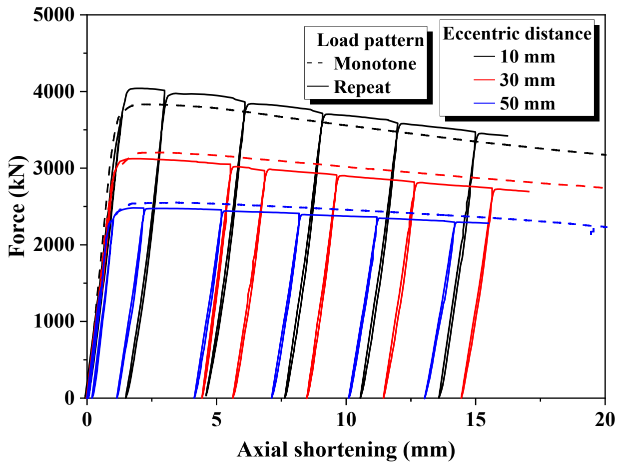

e). D168T10CA15

Fig.6. Force–axial shortening curves of UHPCFSTs under monotonic and repeated eccentric compressions

The force of the peak point in the curve is defined as the eccentric compressive bearing capacity. It is apparent that specimens with smaller eccentricity and thicker steel tube exhibit higher eccentric compressive bearing capacity. Comparing different loading patterns, the bearing capacities of the UHPCFST specimens under repeated loading are lower than those of the specimens under monotonic loading, which can be attributed to the additional damage accumulated in the repeated loading process. More specifically, the damage includes tensile crack and compressive crash of UHPC infill and the development of internal defects of steel. The eccentric compressive stiffness is defined as the slope of the force-axial shortening curve. There are four different kinds of stiffness are investigated in this paper, including initial, decreasing, unloading and reloading compressive stiffness, and they are defined as the slopes of N-Δ curve for linear, decreasing, unloading and reloading phases respectively, those phases are mentioned as last paragraph. Specimens with smaller eccentricity and thicker steel tube exhibit higher initial eccentric compressive stiffness. Conversely, a smaller decreasing compressive stiffness is observed in specimens with higher eccentricity and confinement factor. In UHPCFST, concrete is in a tri-compressive state, when the confinement factor is higher, a greater compressive radial force is acted on the UHPC. Consequently, the ductility of the concrete increases significantly, resulting in a higher residual force of concrete in decreasing phase at same axial shortening, causing a smaller observed decreasing compressive stiffness. For unloading and reloading stiffness, due to the near overlap of the unloading and reloading curves, these two stiffnesses should be similar. As the loading process progresses, the unloading and reloading stiffnesses decrease gradually. In terms of design parameter effects, specimens with a thicker steel tube exhibit higher unloading and reloading stiffnesses. This may be attributed to the reduced volume of concrete in the specimens with thicker steel. Furthermore, Fig.6 shows that the monotonic loading curves are close to the load envelopes of the respective repeated compressive loading curves.

3.1.3. Mid-height section vertical strain distribution

As mentioned in Section 2.3, five pairs of strain gauges are attached to the middle-height section of the steel tube to monitor the real-time strain distribution during the tests. Fig.7 illustrates the vertical strain distribution at 0.2, 0.3, 0.4, 0.5, 0.6, 0.7 and 0.8 of the eccentric compressive bearing capacity before reaching the peak. All vertical strain distributions exhibit a nearly linear relationship with the position within the section, consistent with the common assumption of a flat cross-section.

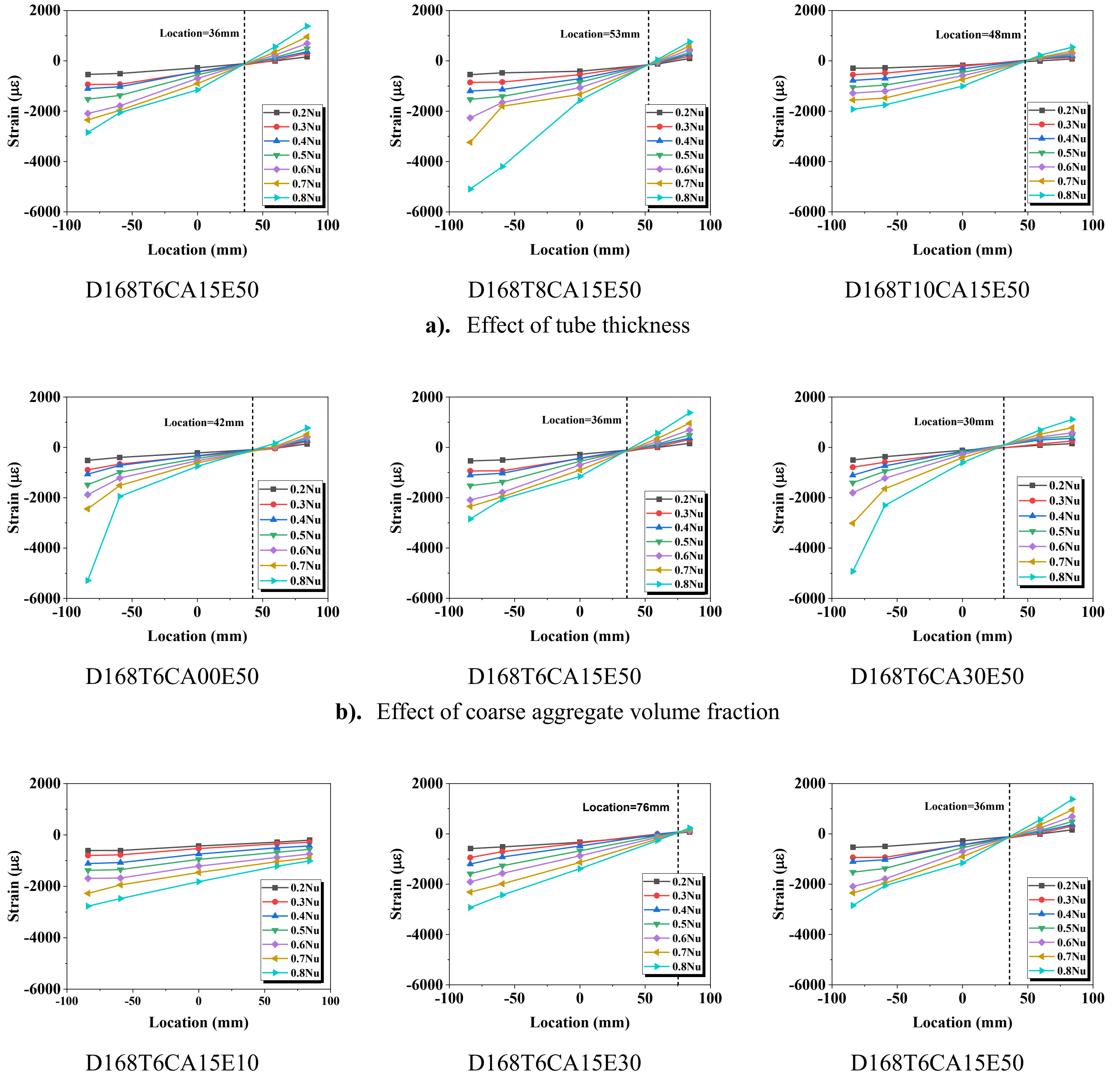

D168T6CA15E50 D168T8CA15E50 D168T10CA15E50

a). Effect of tube thickness

D168T6CA00E50 D168T6CA15E50 D168T6CA30E50

b). Effect of coarse aggregate volume fraction

D168T6CA15E10 D168T6CA15E30 D168T6CA15E50

c). Effect of eccentricity

Fig.7. Strain distribution on the mid-height section of the specimens

Fig.7a) shows the effect of tube thickness on the vertical strain distribution of the mid-height section, it can be found that a specimen with thinner tube tend to have larger tensile strain on the tensile side. Eccentricity also has a significant effect on the strain distribution. When the eccentricity is small, the vertical strains across the entire section are negative, indicating that the entire section is under compression. As the eccentricity increases, as shown in Fig.7c), the part of the section under tension increases. As marked in Fig.7, it is evident that the neural axis shifts to the compressive side of the section as volume fraction of coarse aggregate of UHPC increases. This shift occurs because a higher aggregate content results in more Interfacial Transition Zones (ITZ) in the UHPC, which leads to reduced tensile strength. Consequently, more tensile cracks developed on the tensile side the section, causing further shift of the neural axial shift to the compressive side. For a specimen with thicker tube, on the tensile side of the section, thicker tube results in reduced stress and fewer cracks in the UHPC, and the location of neural axis shift closer to tensile side.

3.1.4. Lateral deflection distribution

The five LVDTs are positioned along the specimen height to measure the real-time lateral deflections during the tests. Fig.8 illustrates the lateral deflection distribution at 0.3, 0.5, 0.7 and 0.9 of the eccentric compressive bearing capacity before reaching the peak. The deflection at the middle height of the specimen consistently exhibits the greatest magnitude compared to that of other locations. The deflections at one-fourth and three-fourth of the specimen height are very similar, while the deflections at both ends remain close to zero. The deflection data are fitted both sinusoidally and parabolically in Fig.8 to show its distribution along the height of the specimen. It is evident that both the sinusoidal and the parabolical functions are sufficiently accurate to describe the deflection of the specimen, and parabolical function outperforms sinusoidal function.

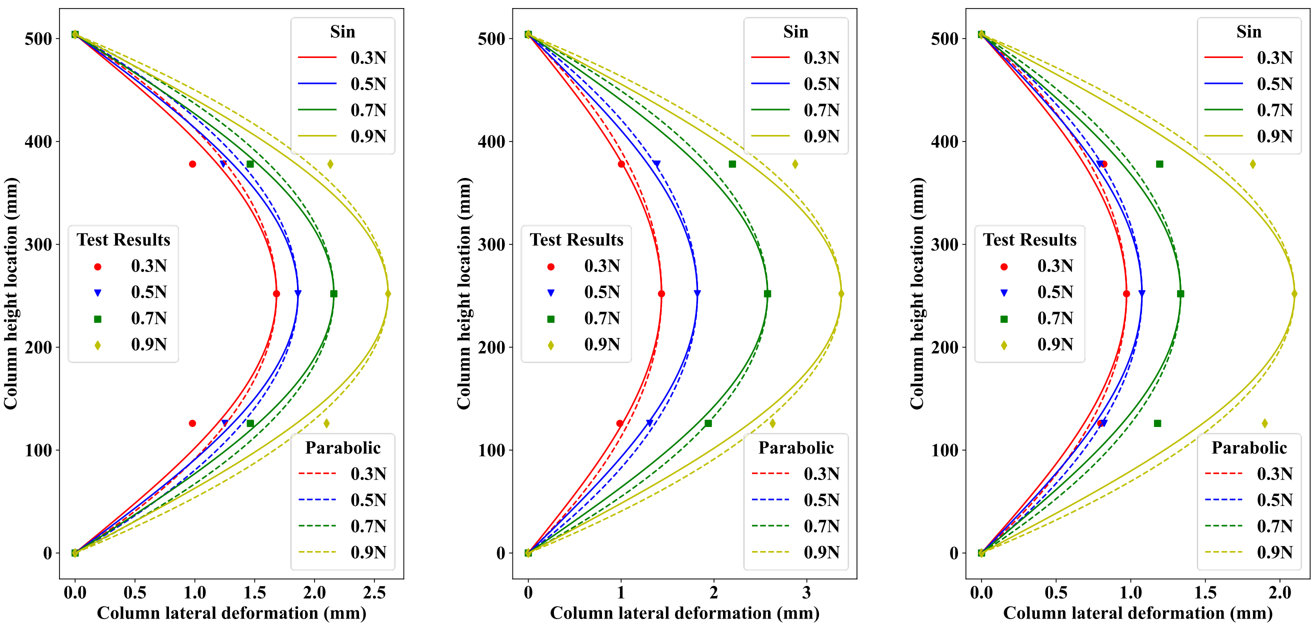

D168T6CA15E10 D168T6CA15E30 D168T6CA15E50

a). Effect of eccentricity

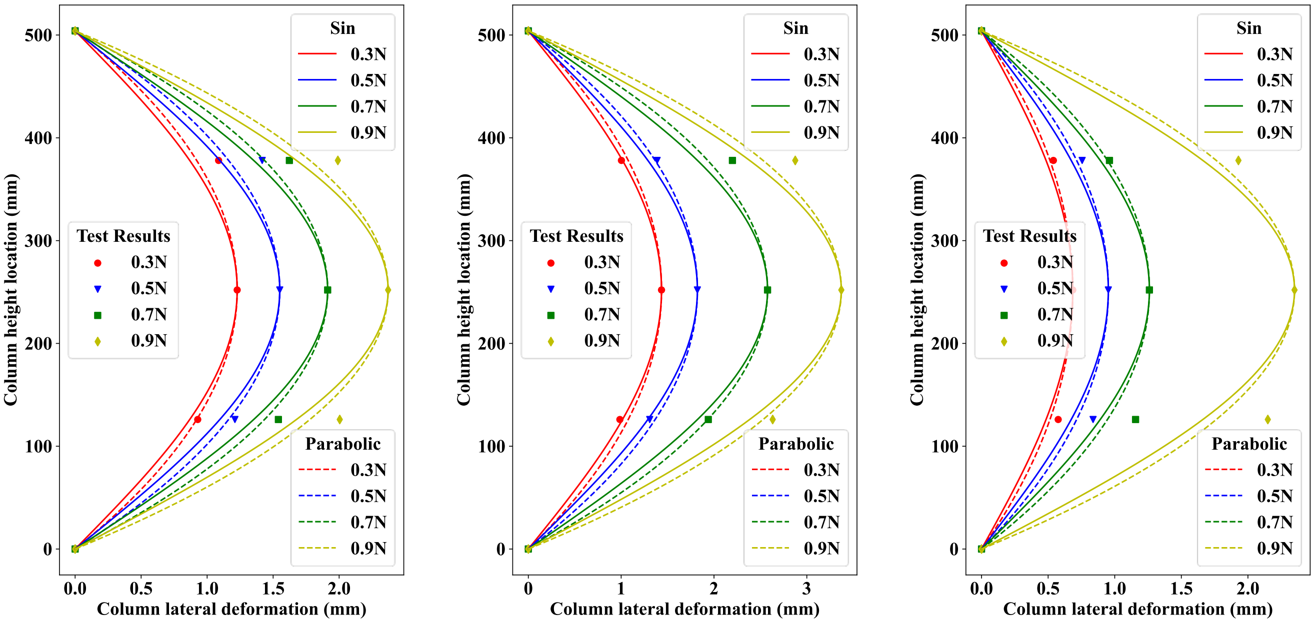

D168T6CA00E30 D168T6CA15E30 D168T6CA30E30

b). Effect of coarse aggregate volume fraction

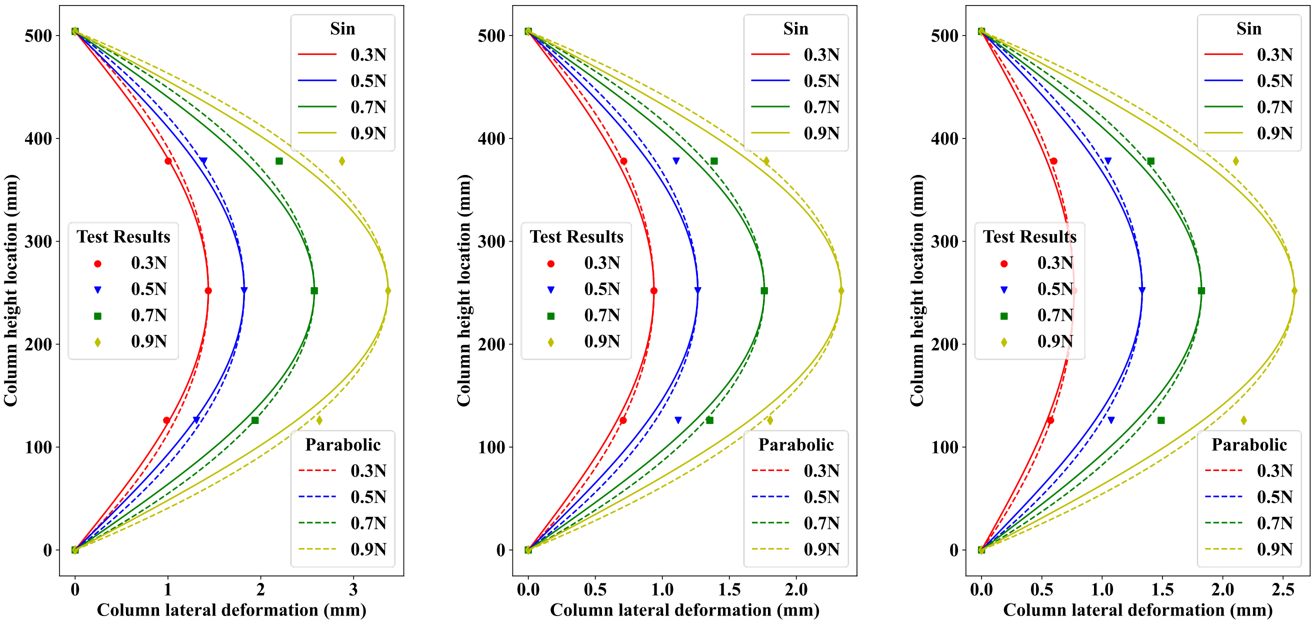

D168T6CA15E30 D168T8CA15E30 D168T10CA15E30

c). Effect of tube thickness

Fig.8. Lateral deflection along the height direction

3.2. Results analysis

3.2.1. Eccentric compressive bearing capacity and initial eccentric compressive stiffness

Eccentric compressive bearing capacity and initial eccentric compressive stiffness are two of the most important values that evaluate the mechanical properties of a component under eccentric loading. In this section, these two values are calculated, and the effects of design parameters are quantitatively analyzed.

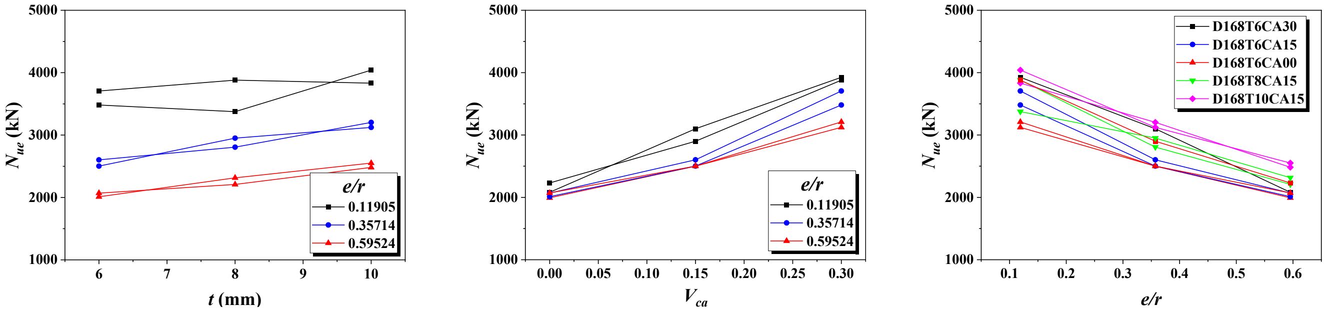

a). Steel tube thickness

b). Coarse aggregate volume fraction of UHPC

c). Eccentricity

Fig.9. Eccentric compressive bearing capacity of the UHPCFST specimens

In this paper, eccentric compressive bearing capacity (N_{ue}) of the UHPCFST is defined as the peak compressive force of the N-Δ curve. Fig.9 shows the eccentric compressive bearing capacity of the UHPCFST specimens with different eccentricities, steel tube diameters and coarse aggregate volume fractions. Regardless of whether they are monotonically or repeatedly loaded, the eccentric compressive bearing capacity of the UHPCFST significantly increases with the increases of thickness of the steel tube and coarse aggregate volume fraction of the UHPC. The eccentric compressive bearing capacity of the UHPCFST decreases significantly, however, as the eccentricity increases.

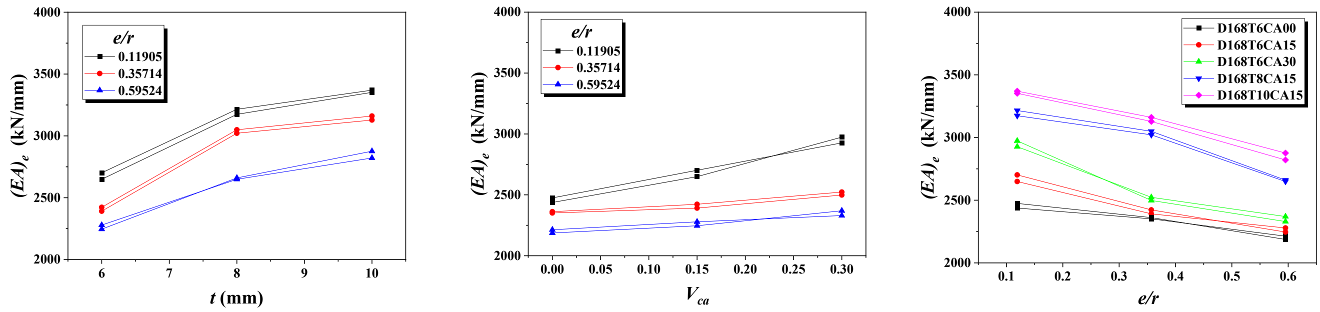

a). Eccentricity Steel tube thickness

b). Coarse aggregate volume fraction of UHPC

c). Eccentricity

Fig.10. Eccentric compressive stiffness of the UHPCFST specimens

The impact of the design variables of the specimen on the initial eccentric compressive stiffness is similar to its effect on the axial compressive bearing capacity, as illustrated in Fig.9 and Fig.10. As the thickness of the steel tube and coarse aggregate volume fraction of UHPC increases, the initial stiffness also increases. As the eccentricity increases, the initial stiffness decreases.

3.2.2. Unloading and reloading stiffness degradation

During an earthquake, structural components undergo multiple cycles of repeated loading, leading to accumulated damage and resulting in the deterioration of their mechanical properties, including a decrease in stiffness and bearing capacity. Through repeated eccentric compressive load tests, the degradation of stiffness can be investigated by analysis unloading and reloading stiffness. Upon examining each unloading and reloading cycle, it can be found that the reloading stiffness is slightly bigger than the unloading stiffness (< 5%). In this section, the reloading stiffness is employed to evaluate the degradation of eccentric compressive stiffness in UHPCFST subjected to eccentric compression.

Fig.11 shows the reloading stiffness-axial shortening curve of the UHPCFST specimens with respected to their eccentricity, steel tube thickness and coarse aggregate. With the increase of axial shortening, the reload stiffness of all specimens gradually decreases. The rate of stiffness reduction highly depends on the above design factors. Specimens with a larger eccentric loading, more coarse aggregate and thinner steel tube exhibit a higher rate stiffness degradation.

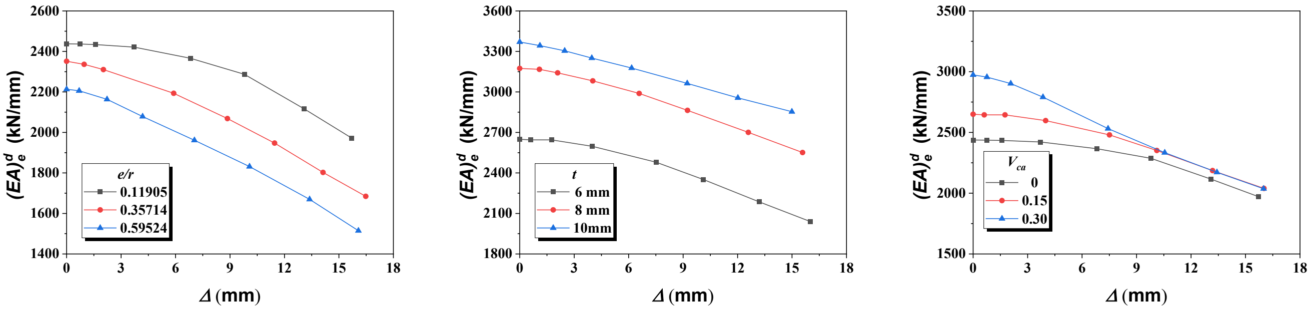

a). Eccentricity **b).** Steel tube thickness **c).** V_{ca}

Fig.11. Stiffness degradation of the UHPCFST under eccentric compression

To quantitatively investigate stiffness degradation in the UHPCFST under eccentric compressive load, a stiffness reduction factor (k_{stiff}^{d}) is introduced and can be calculated using Eq. (1), where $K_{unloading\{i\}}$ represents the reloading stiffness of the i-th unloading and reloading cycle, $K_{initial_{initial}}$ represents the initial stiffness of the specimen.

$$k_{stiff}^{d} = K_{unloading\{i\}}/K_{initial} \tag{1}$$

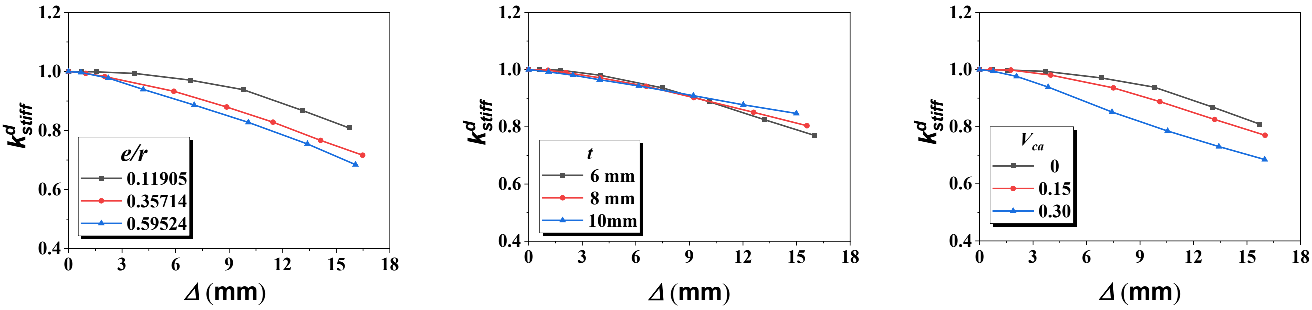

a). Eccentric distance **b).** Steel tube thickness **c).** V_{ca}

Fig.12. Stiffness degradation of the specimens

Fig.12 illustrates the relationship between the stiffness reduction factor (k_{stiff}^{d}) and the unloading axial shortening for repeated eccentric compressive specimens. It can be observed that tube thickness, coarse aggregate volume fraction, and eccentricity all have an impact on k_{stiff}^{d}. Specimens with thicker steel tubes show less stiffness degradation. This is because the mechanical properties of UHPC decrease more significantly than those of steel during the loading process, and the specimens with thicker steel tubes have a lower proportion of UHPC. Regarding the coarse aggregate volume fraction, the UHPC with a higher proportion of coarse aggregate is more prone to cracking, indicating more damage within the UHPC. The specimens with a lower coarse aggregate volume fraction demonstrate a less pronounced tendency of stiffness degradation. Fig.12a) displays the relationship between stiffness degradation and eccentric distance. Specimens loaded with bigger eccentric distance exhibit severe stiffness degradation. As mentioned in Section 3.1.1, specimens with a larger eccentricity tend to exhibit more severe compressive crushing and tensile cracking in the UHPC infill, which can explain the severe stiffness degradation.

4. Calculation method of eccentric compressive mechanical performance of UHPCFST

4.1. Empirical model of force-axial shortening curve

The force-axial shortening curve serves as one of the most valuable characteristics for understanding the mechanical behavior of UHPCFST under eccentric compression. It is vital for predicting structural response, and optimizing UHPCFST designs. In this section, we construct an empirical force-axial shortening curve for UHPCFST under eccentric compression.

The empirical force-axial shortening curve for UHPCFST comprises two parts: the envelope curve and the unload and reload path, as seen in Fig.13.

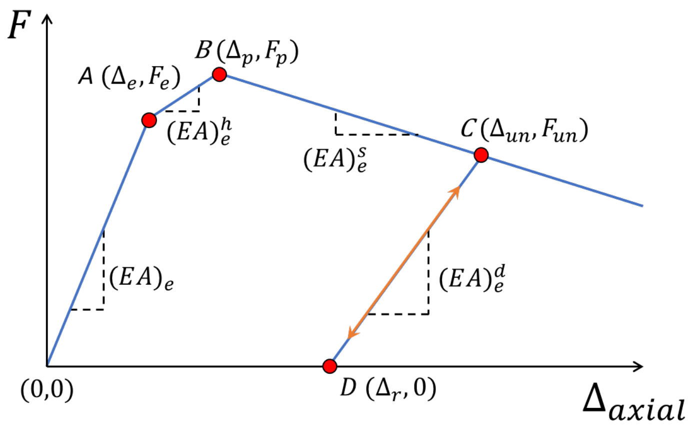

Fig.13. Empirical model for UHPCFST under eccentric compressive loading.

The envelope curve is used to describe the mechanical behavior of the structural component under monotonic loads. As discussed in Section 3.1.2, a typical experimental force-axial shortening curve for UHPCFST under monotonic compression consists of three phases, i.e., linear, nonlinear hardening, and softening phases. However, for the purpose of simplification, the nonlinear hardening and softening phase are linearized approximately, as shown in Eq. (2)

$$F = \begin{cases} (EA)_e \Delta & \Delta < \Delta_e \\ F_e + (\Delta - \Delta_e)(EA)_e^h & \Delta_e < \Delta < \Delta_p \\ F_p - (EA)_e^s(\varepsilon - \varepsilon_h) & \Delta_p < \Delta < \Delta_u \end{cases} \quad (2)$$

A linear model with progressively decreasing stiffness is used to characterize the unloading and reloading behavior of UHPCFST under repeated eccentric compression. In Eq. (3), $\mathrm{F_{un}}$ represents the unloading force, and Δ_{un} denotes the last unloading axial shortening. The reduced section stiffness, $(EA)_e^d$, can be calculated using the original section stiffness, $(EA)_c$, and the stiffness reduction factor k_{stiff}^d introduced.

$$F = F_{un} - (EA)_e^d(\Delta - \Delta_{un}) \qquad \Delta < \Delta_{un} \quad (3)$$

To construct this empirical model, there are keys parameters needs to be determined for each phase, seen in Table.5. Eccentric compressive bearing capacity (F_p), eccentric compressive stiffness ($(EA)_c$ and $(EA)_e^d$) are discussed in Section 4.2, 4.3.1 and 4.3.2 respectively.

Table.5 Key parameters in proposed empirical model

Phase	Key parameters
Elastic	$(EA)_e$ (Discussed in section 4.3.1) $F_e = 0.8F_p$ $\Delta_e = \dfrac{F_e}{(EA)_e}$
Hardening	F_p (Discussed in section 4.2) $\Delta_p = \Delta_e + \dfrac{0.2F_p}{(EA)_e} e^{\xi + \frac{e}{r}}$
Softening	$(EA)_e^s = \dfrac{A_sE_s + A_cE_c}{L} \dfrac{0.012}{e^{1.08\xi + \frac{e}{r}} - 1.3}$
Unloading and reloading	$(EA)_e^d$ (Discussed in section 4.3.2)

The remaining parameters of the empirical models are determined through regression analysis. To ensure the generality of the model, the test specimens are divided into two sets: one for formula regression (24 specimens) and another for validation (6 specimens). The formula regression set is used to determine the unknown factors in the formulas via regression analysis. The validation set is to evaluate the applicability and generalization of the proposed empirical model. Through the regression analysis, the remaining parameters in the above empirical models can be calculated using the formulas inTable.5.

4.2. Eccentric compressive bearing capacity F_p

There are two approaches to calculate eccentric compressive bearing capacity of UHPCFST, as illustrated in Fig.14. The first approach uses an eccentric reduction factor to calculate the eccentric compressive bearing capacity from the axial compressive bearing capacity without considering eccentricity. Another approach is to find the intersection between the N-M curve and an inclined straight line. To calculate the eccentric compressive capacity of a column with eccentricity e using sectional N-M curves, the sectional moment M should be equal to the sectional force N multiplied by the eccentricity e. Additionally, the point (N, M) should lie on the N-M curve. Therefore, an inclined straight line with a slope of e is applied to intersect the N-M curve. The N value at the intersection point is considered the eccentric compressive capacity of the column.

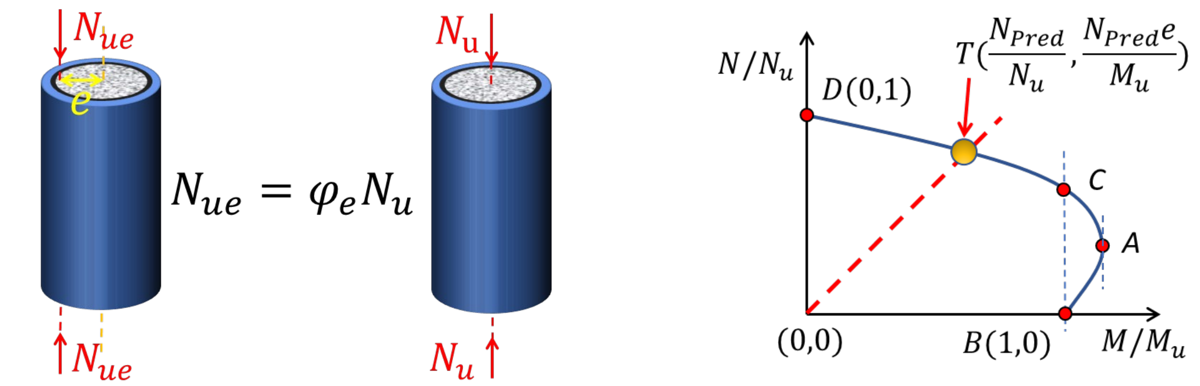

a). Approach 1: Eccentric loading reduction factor **b).** Approach 2: N-M curve intersection

Fig.14. Prediction method for eccentric compressive bearing capacity of columns

4.2.1. Analysis and evaluation of existed formulas for traditional CFST

Table 6 presents some of the existing formulas that are used frequently to predict the N-M curve of CFST.

Table.6 N-M curves formulas and code provisions

Source	Form of N-M curve	Formula	Related Bearing capacity
Yu[33]	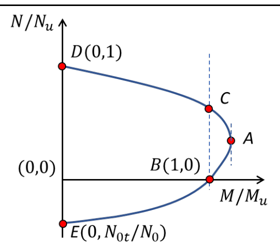	$\frac{M}{M_u} = \left(1 - \frac{N}{N_u}\right)\left(1 - \frac{N}{N_{ut}}\right)$	$M_u = \left(1 - \frac{1}{4}\frac{\xi}{\xi + 1}\right) f_y A_s R$ $N_u = A_s f_y + A_c f_c$ $N_{ut} = 1.1 A_s f_y$
Han[7]	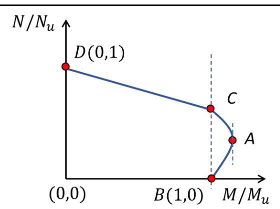	$\begin{cases} \frac{N}{N_u} + a\frac{M}{M_u} = 1 & \frac{N}{N_u} \geq 2\eta_0 \\ -b\left(\frac{N}{N_u}\right)^2 - c\frac{N}{N_u} + \frac{M}{M_u} = 1 & \frac{N}{N_u} < 2\eta_0 \end{cases}$	$N_u = (A_s + A_c) f_{sy}$ $M_u = \gamma_m W_{scm} f_{scy}$

AISC 360[34]	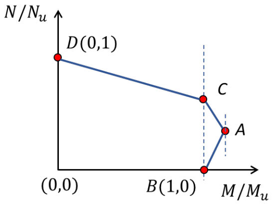	$\begin{cases} \frac{N}{N_u} + a\frac{M}{M_u} = 1 & \frac{N}{N_u} \geq 2\eta_0 \\ b\frac{N}{N_u} + c\frac{M}{M_u} = 1 & 2\eta_0 > \frac{N}{N_u} \geq \eta_0 \\ d\frac{N}{N_u} + \frac{M}{M_u} = 1 & \frac{N}{N_u} < \eta_0 \end{cases}$	$N_u = A_s f_y + A_c 0.85 f_c$ $M_u = W_{psn} f_y + 0.5 W_{pcn} 0.85 f_c$
EC4[35]			$N_u = A_s f_y + A_c f_c$ $M_u = W_{psn} f_y + 0.5 W_{pcn} f_c$
GB50936-2014 [36]	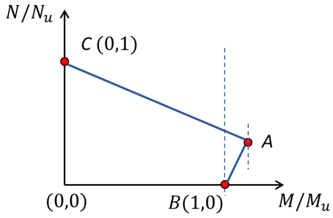	$N_{ue} = \varphi_e N_u$ $N_u = \begin{cases} 0.9A_c f_c(1+\alpha\xi) & \xi \leq \frac{1}{(\alpha-1)^2} \\ 0.9A_c f_c(1+\sqrt{\xi}+\xi) & \xi > \frac{1}{(\alpha-1)^2} \end{cases}$ Approach 2 (above) is converted to approach 1(below)[37] $\begin{cases} \frac{N}{N_u} + 0.555\frac{M}{M_u} \leqslant 1 & \frac{N}{N_u} \geqslant 0.255 \\ \frac{1-\frac{4}{3}}{0.255}\frac{N}{N_u} + \frac{M}{M_u} \leqslant 1 & \frac{N}{N_u} < 0.255 \end{cases}$	$N_u = A_{sc} f_{sc}$ $M_u = 0.3 r_c N_0$

In Table.6,. N_u denotes eccentric compressive capacity; M_u denotes ultimate flexural capacity, N_{ut} denotes tensile capacity. φ_e denotes bearing capacity reduction factor that considers eccentric loading; N_0 denotes axial compressive capacity; ξ denotes confinement factor; e_0 denotes total loading eccentricity on critical section, r_0 denotes radius of steel tube; and α is a factor that related to concrete grade. w_{scm} is section module of CFST section; w_{psn} is plastic section module of steel tube; w_{pcn} is plastic section module of concrete

Comparing the above N-M curves, the selection of different N-M curves and bearing capacity formulas leads to different prediction results. For N-M curves, AISC and EC4 adopt a three-phase straight-line model, which is the most complex one. Han and GB50936-2014 present a two-stage model. Of which GB50936 assumes both stages are linear, while the second stage of Han's model is nonlinear. Yu's model is the simplest with only one equation.

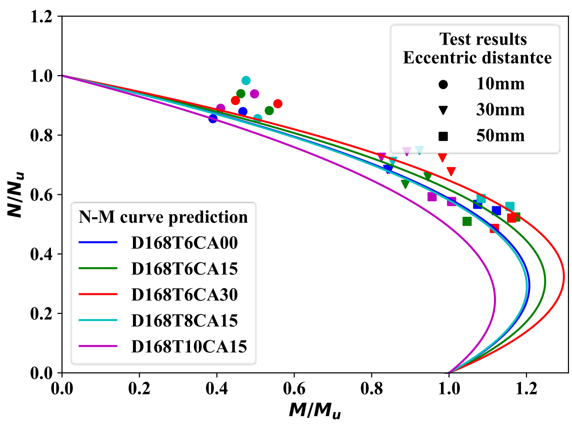

i). N-M curve prediction

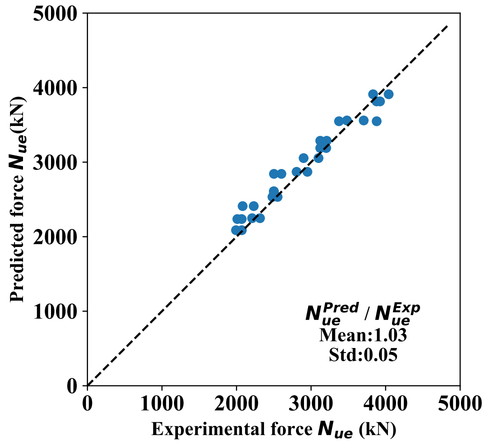

ii). Eccentric compressive bearing capacity prediction

a). Yu

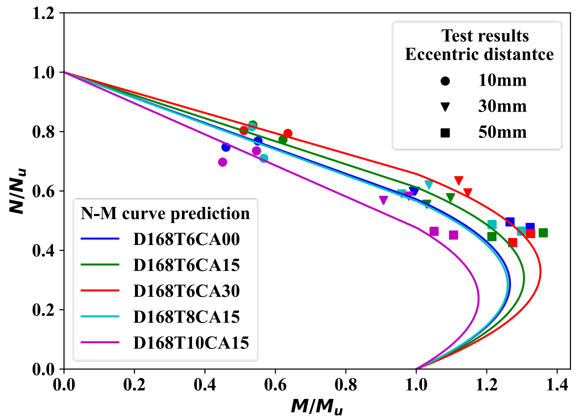

i). N-M curve prediction

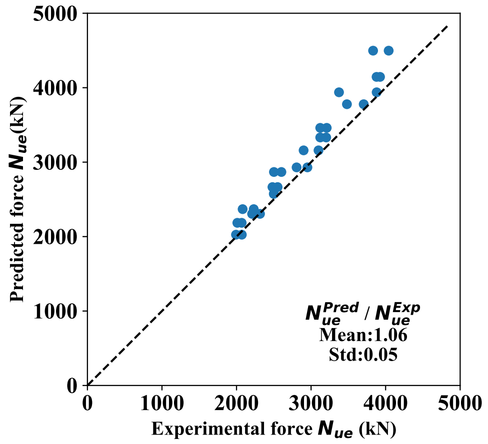

ii). Eccentric compressive bearing capacity prediction

b). Han

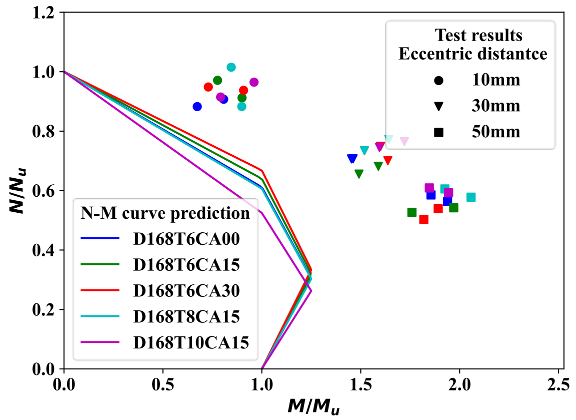

i). N-M curve prediction

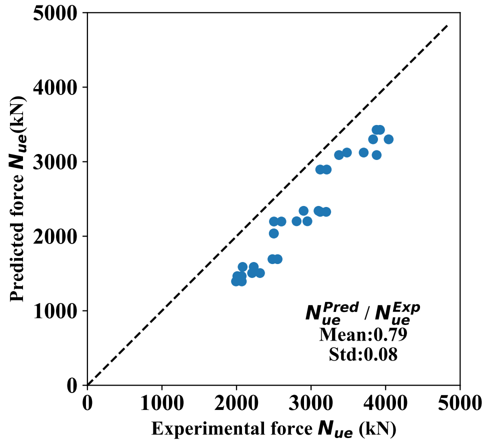

ii). Eccentric compressive bearing capacity prediction

c). AISC360-10

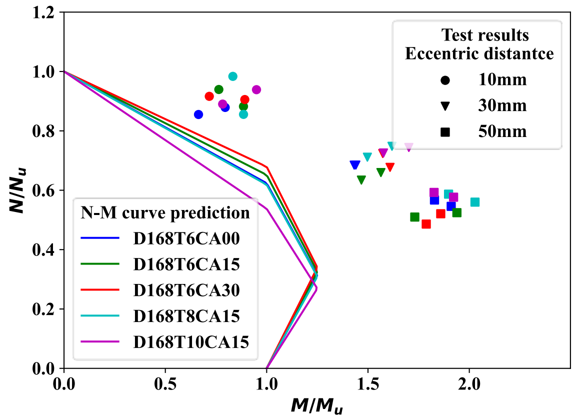

i). N-M curve prediction

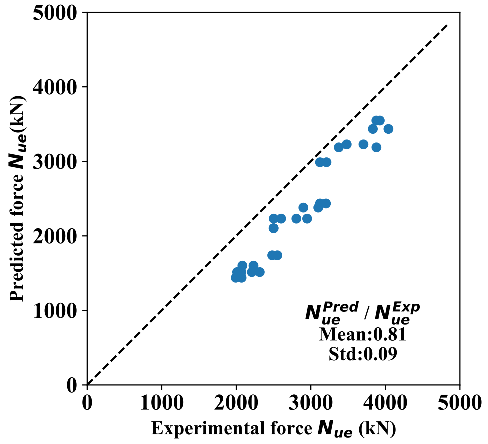

ii). Eccentric compressive bearing capacity prediction

d). EC4

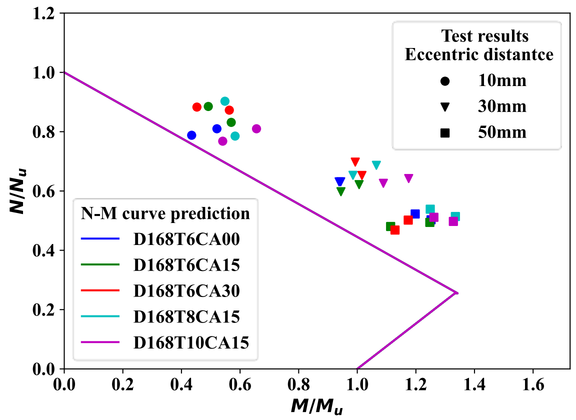

i). N-M curve prediction

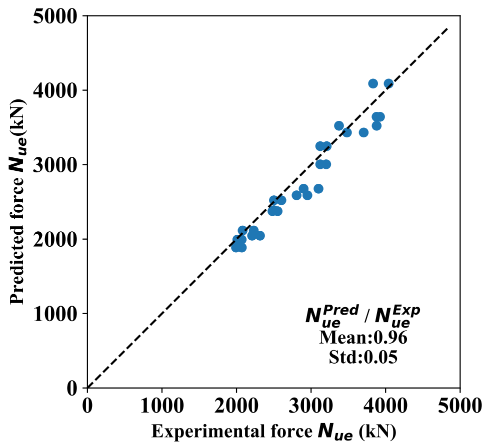

ii). Eccentric compressive bearing capacity prediction

e). GB50936-2014

Fig.15. Existed formulas prediction

Both the predictions of the test specimen on N-M curve and eccentric compressive bearing capacity are presented in Fig.15. For prediction presented in N-M curve, the Yu and Han's N-M curves exhibit good agreement with the test results. Most of the experimental (N and M) points are located outside and close to the respective curves, indicating a safe and economical design and demonstrating the good accuracy of the N-M curves. For the predictions of EC4, AISC, and GB50936-2014, all the experimental (N and M) points are located far outside from the N-M curves, suggesting that the codes have incorporated sufficient safety provisions. Comparing the predicted eccentric compressive capacities with the experimental values, Yu's formula shows the best performance with an average error of 3%. GB50936 ranks second with an average error of 4%, while Han's model ranks fourth with an average error of 6%. EC4 and AISC significantly underestimate the eccentric compressive capacity of the UHPCFST tested in this study, with an error approaching 20%.

4.2.2. Calibrated formulas for UHPCFST

However, the previously mentioned formulas are designed for CFST rather than UHPCFST, or they cannot provide very good predictions for the N-M curve of UHPCFST. Therefore, for the sake of simplicity, Yu's N-M curve formula form, Eq (4), is adopted for calibration.

$$\frac{M}{M_u} = \left(1 - \frac{N}{N_u}\right)\left(1 - \frac{N}{N_{ut}}\right) \tag{4}$$

According to previous investigates on repeated axial compressive[38] and tensile[39] mechanical performance of UHPCFST. Eqs. (5) and Eq (6) are validated and can give the precise predictions on axial compressive and tensile bearing capacity of UHPCFST, which are applied in the propose N-M formulas for prediction of N_u and N_{ut}.

$$N_0 = \left(1 + \alpha\frac{\xi_u}{1 + \xi_u}\right)\left[A_c(\gamma_u f_{ck}) + A_s f_y\right]$$
$$\gamma_u = \left(\frac{d}{168}\right)^{0.11} \quad \xi_u = \frac{f_y A_s}{(\gamma_u f_c)A_c} \tag{5}$$

$$N_{0t} = 1.1 f_y A_s \tag{6}$$

Regarding the ultimate flexural capacity of UHPCFST, Wu [30] propose a formula for UHPCFST and this formula can provide precise predictions of the ultimate flexural capacity of UHPCFST. Therefore, the ultimate flexural capacity in Yu's model, adopts Wu's formulas, as shown in Eq. (7).

$$M_u = \left(1 - \frac{1}{4}\frac{\xi}{\xi + 1}\right) f_y A_s R \tag{7}$$

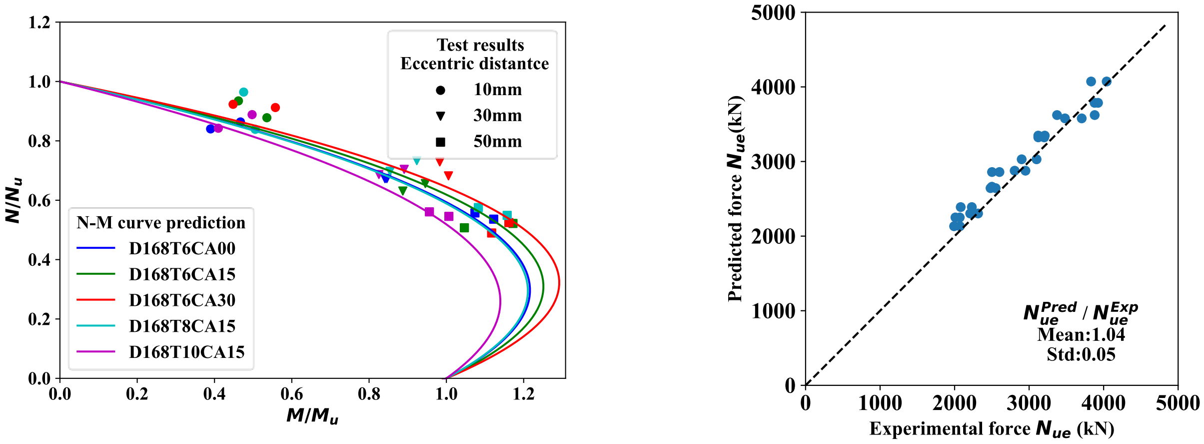

a). N-M curve prediction **b).** Eccentric compressive bearing capacity prediction

Fig.16. Code predictions of the eccentric compressive bearing capacity

With formulas proposed above, the N-M curve prediction and predicted eccentric compressive bearing capacity of the tested specimens are shown in Fig.16. The proposed formulas show a good predictive capability for the eccentric compressive capacity of UHPCFST and is selected for the construction of the force-axial shortening empirical model.

4.3. Eccentric compressive stiffness

In this section, a formula for predicting initial eccentric compressive stiffness is developed. Moreover, an exponential equation is constructed to calculate stiffness degradation mentioned in section 3.2.2

4.3.1. Initial eccentric compressive stiffness $(EA)_e$

Based on the test results of the lateral deformation in Section 3.1.4, parabolic function can effectively represent the distribution of lateral deformation. Fig.17 illustrates the schematic geometry of both unloaded and loaded components under eccentric compression, demonstrating a parabolic distribution. Previous literature[40] provides Eqs.(8) to (10) for calculating lateral deformation, mid-height lateral deformation, and axial shortening.

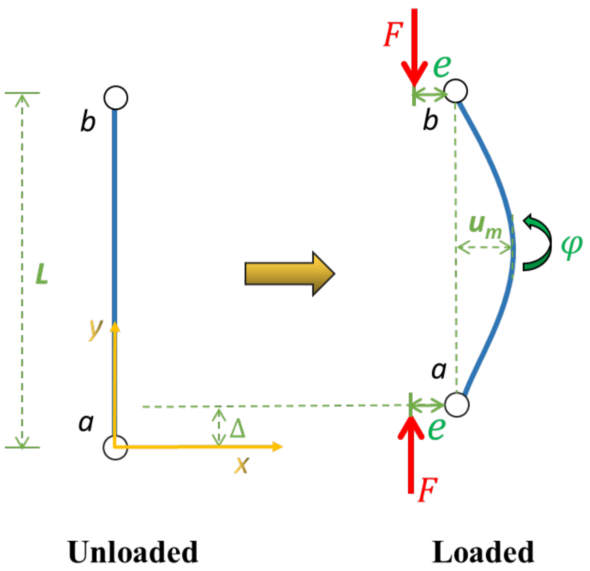

Parabolic function assumption:

Basic formulas

$$y = -\frac{4u_m}{(L-\Delta)^2}(x-(L-\Delta))x \tag{8}$$

$$u_m = \varphi\frac{L^2}{8} \tag{9}$$

$$\Delta = 8\frac{{u_m}^2}{3L} + \varepsilon L \tag{10}$$

Fig.17. Deformation

The moment on the mid-height can be calculated from the Force (F), eccentricity (e) and lateral deformation (u_m), as shown in Eq. (11).

$$M = F(e+u_m) \tag{11}$$

Combining Eq. (9) and Eq. (11), the curvature of the mid-height section (φ) can be calculated by Eq.(12).

$$\varphi = \frac{M}{EI} = \frac{F(e+u_m)}{EI} = \frac{F\left(e+\varphi\frac{L^2}{8}\right)}{EI} \tag{12}$$

The mid-height curvature (φ) can be obtained by solving Eq. (6), and is shown in Eq. (13).

$$\varphi = \frac{8Fe}{8EI - FL^2} \tag{13}$$

Introducing the mid-height curvature to Eq. (9), the mid-height lateral deformation can be calculated as,

$$u_m = \varphi\frac{L^2}{8} = \frac{FL^2e}{8EI - FL^2} \tag{14}$$

As shown in Eq. (10), the axial shortening consists of two components, i.e., the deformation caused by bending and the deformation caused by axial compression. The former can be calculated based on Eq. (14) and the latter can be obtained from the imposed force and the sectional module of the component as shown in Eq. (15).

$$\varepsilon = \frac{F}{EA} \qquad F = EA\varepsilon, \tag{15}$$

Finally, Eq. (16) is constructed to calculate the axial shortening.

$$\Delta = 8\frac{{u_m}^2}{3L} + \varepsilon L = \frac{8}{3}\frac{F^2L^3e^2}{(8EI - FL^2)^2} + \frac{FL}{EA} \tag{16}$$

To calculate the stiffness, which is $\frac{F}{\Delta}$, F needs to be solved from Eq. (16). However, the Eq. (16) is a quadratic polynomial of F, which is too complex to solve. Here $\frac{F}{\Delta}$ is constructed.

$$\frac{F}{\Delta} = \frac{F}{\frac{8}{3}\frac{F^2L^3e^2}{(8EI - FL^2)^2} + \frac{FL}{EA}} \tag{17}$$

In this paper, the section of all specimens is circular. Thus, the sectional areas (A) and the sectional 2nd moment of area, can be calculated by

$$A = \pi r^2$$
$$I = \frac{\pi}{4}r^4 \tag{18}$$

Introducing Eqs (18) and (15). to Eq.(17) yields the following.

$$\frac{F}{\Delta} = \frac{EA}{L}\frac{1}{1 + \frac{8}{3}\frac{\left(\frac{L}{r}\right)^2\left(\frac{e}{r}\right)^2\varepsilon}{\left(2 - \varepsilon\left(\frac{L}{r}\right)^2\right)^2}} \tag{19}$$

All the above equations were derived by assuming that the column is always elastic and the modules remain constant. To consider plastic and damage development in the loading process, factors α and β are applied here to replace the constant factor in Eq.(19), as shown in Eq.(20). The determination of the factor, α and β, are through calibrations from experimental results.

$$\frac{\partial F}{\partial \Delta} = \frac{EA}{L} \frac{1}{1 + \frac{\beta \left(\frac{L}{r}\right)^2 \left(\frac{e}{r}\right)^2}{\left(2 - \alpha \left(\frac{L}{r}\right)^2\right)^2}} \tag{20}$$

From Eq. (20), an increase of *L/r* or *e/r* will result in a decrease of stiffness, which is consistent with the experimental observation.

In this paper, the section module can be calculated as the superposition of the section modules of concrete and steel tube. i.e., $EA = A_s E_s + A_c E_c$. The factors α and β are 0.18 and 0.93, respectively, determined through numerical regression using the experimental results from the regression group in this study.

To verify the wider applicability of the proposed equation, the fiber model method[41] is employed to generate a set of simulated specimens. As illustrated in Fig.18 a), the fiber model provides accurate predictions of eccentric compressive stiffness. Table 7 shows the parameters of the 225 simulated specimens.

Table.7 Parameter selection of expanded simulation specimen set

d	t/d	e/r	l/d
100, 200, 300, 400, 500	0.02, 0.04, 0.06, 0.08, 0.1	0.2, 0.4, 0.6	3, 6, 9

In Table.7,. d is the diameter of steel tube, t is the thickness of steel tube, e is the loading eccentricity and l is the length of specimen.

In Fig.18 b), a comparison between the simulated stiffness and the predicted stiffness from the formula indicates that the proposed model provides a satisfactory prediction of the eccentric compressive stiffness. The ratio between simulated stiffness and formula-calculated stiffness is used to evaluate the predictive capacity of the formulas. For the predictions of the test sets, the mean ratio is 1.03 with a standard deviation of 0.13. For the predictions of the simulated set, the mean ratio is 0.98 with a standard deviation of 0.31. The proposed formulas can be applied to the commonly used parameters range (Table 7) of UHPCFST.

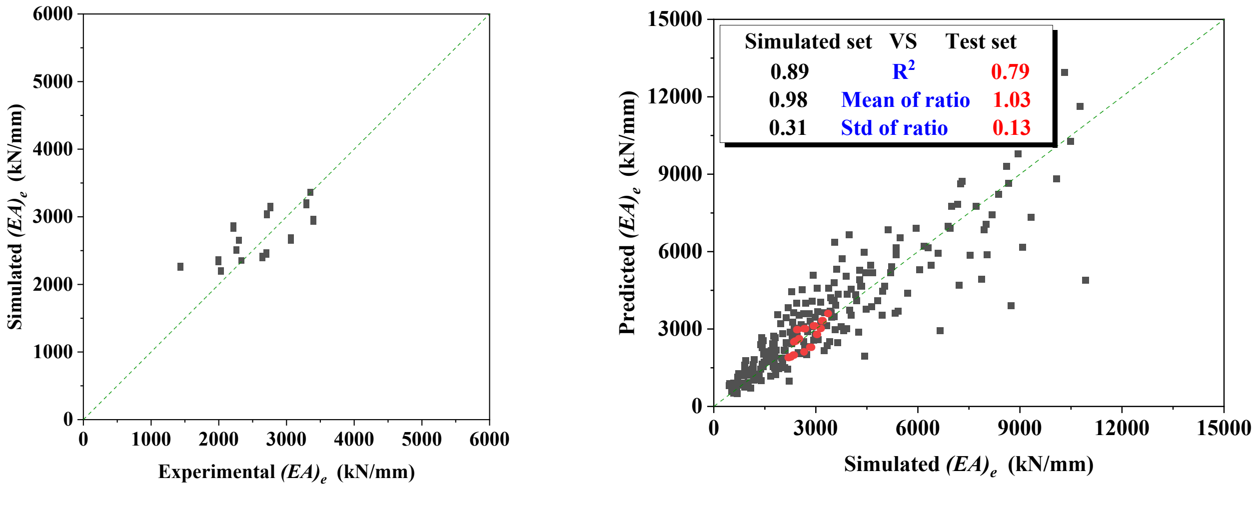

a). Validation of fiber model **b).** Prediction of proposed formula

Fig.18. Evaluation of the proposed formulas for predicting eccentric compressive stiffness of UHPCFST

4.3.2. Degradation of eccentric compressive stiffness $(EA)_e^d$

In Section 3.2.20, stiffness degradation of UHPCFST under eccentric compression is observed and analyzed. Due to the absence of a clear theoretical approach for deriving stiffness degradation from traditional damage mechanisms or alternative methods, this article employs an empirical form for simplicity. According to the definition of the stiffness reduction factor in Eq (1), the formula modeling this stiffness reduction factor should pass through (0,1) and exhibit a decreasing trend, with output values ranging between 0 and 1. To meet those constraints, an exponential decreasing formula has been selected here to describe this stiffness degradation, as shown in Eq. (21).

$$(EA)_e^d = k_{stiff}^d(\Delta)(EA)_e$$
$$k_{stiff}^d = e^{-\left(\frac{\Delta/\Delta_p}{\eta}\right)^{\beta}} \qquad (21)$$
$$D = e^{-\left(\frac{\Delta/\Delta_p}{\eta}\right)^{\beta}}$$

By regression using the experimental results of regression set, the two factors, β and η, can be calculated by Eq. (22). As stated previously, the formulas, Eq.(22), presented are empirical and lack physical significance, which constitutes a limitation of this study.

$$\eta = 66.38\xi - 17.48V_{ca} + 0.05\frac{e}{r} - 4.97$$
$$\beta = -1.05\xi - 0.41V_{ca} - 1.12\frac{e}{r} + 2.52 \qquad (22)$$

Fig.19 shows that the proposed formula can give a relatively accurate prediction on the stiffness reduction factor (k_{stiff}^d).

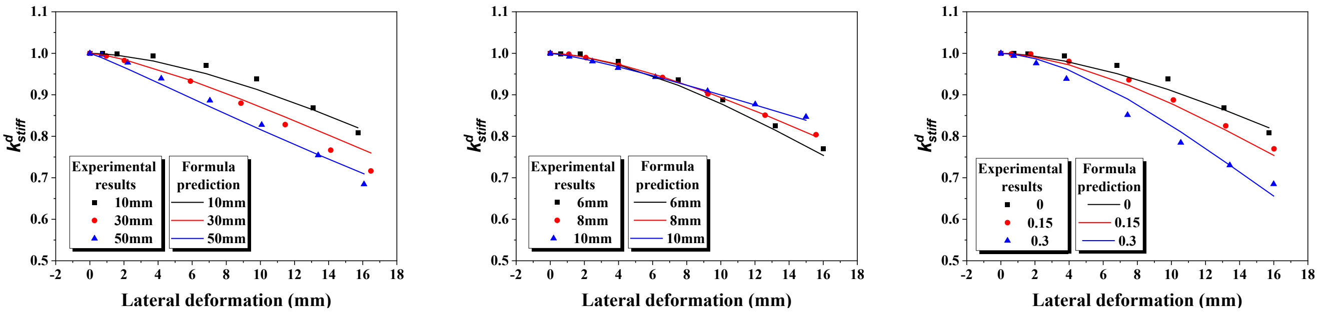

a). Eccentric distance **b).** Steel tube thickness **c).** V_{ca}

Fig.19. Prediction of stiffness degradation

4.4. Empirical model validation

Fig.20 and Fig.21 present comparisons between the predictions of the proposed empirical force-axial shortening formulas and the experimental data obtained from tests for regression and validation sets, respectively.

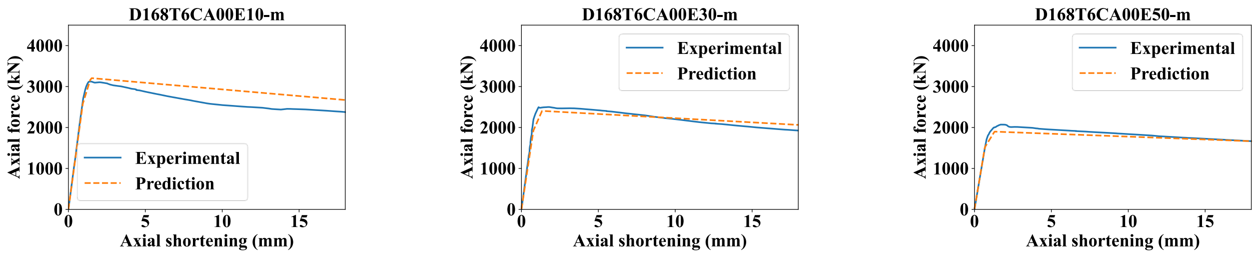

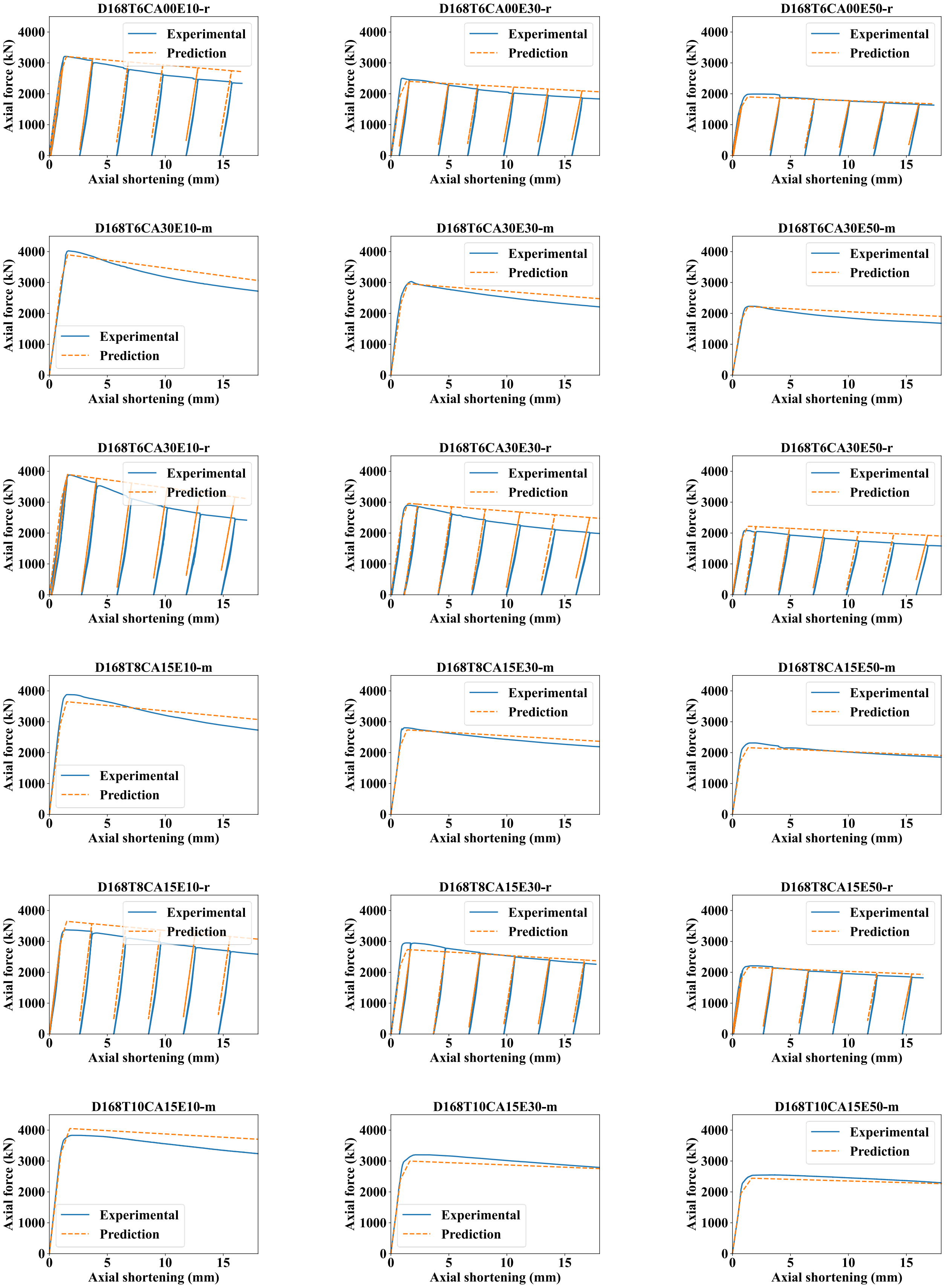
D168T6CA00E10-r
D168T6CA00E30-r
D168T6CA00E50-r
D168T6CA30E10-m
D168T6CA30E30-m
D168T6CA30E50-m
D168T6CA30E10-r
D168T6CA30E30-r
D168T6CA30E50-r
D168T8CA15E10-m
D168T8CA15E30-m
D168T8CA15E50-m
D168T8CA15E10-r
D168T8CA15E30-r
D168T8CA15E50-r
D168T10CA15E10-m
D168T10CA15E30-m
D168T10CA15E50-m
Experimental
Prediction
Axial force (kN)
Axial shortening (mm)
0
1000
2000
3000
4000
5
10
15

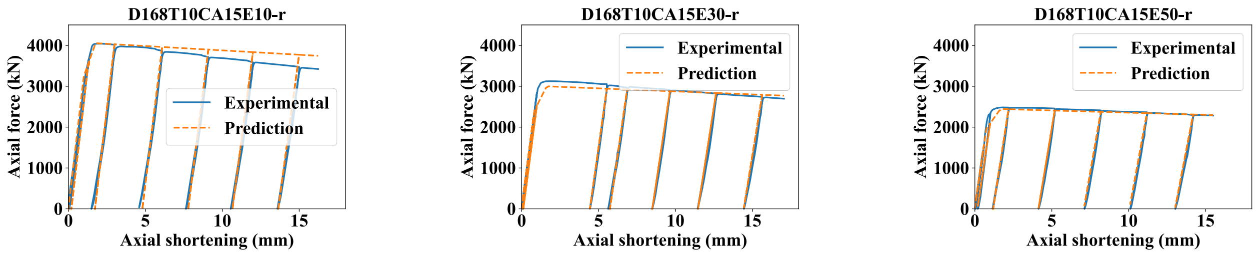

Fig.20. Prediction of the proposed empirical model on formulas regression set

Compared to the experimental results used in both the regression and the validation set, the force-axial shortening model proposed in this paper accurately predicts the force-axial shortening curves under monotonic loading and the skeleton force-axial shortening curves from repeated loading tests. Additionally, it offers accurate predictions for the unloading and reloading curves observed in the repeated loading tests.

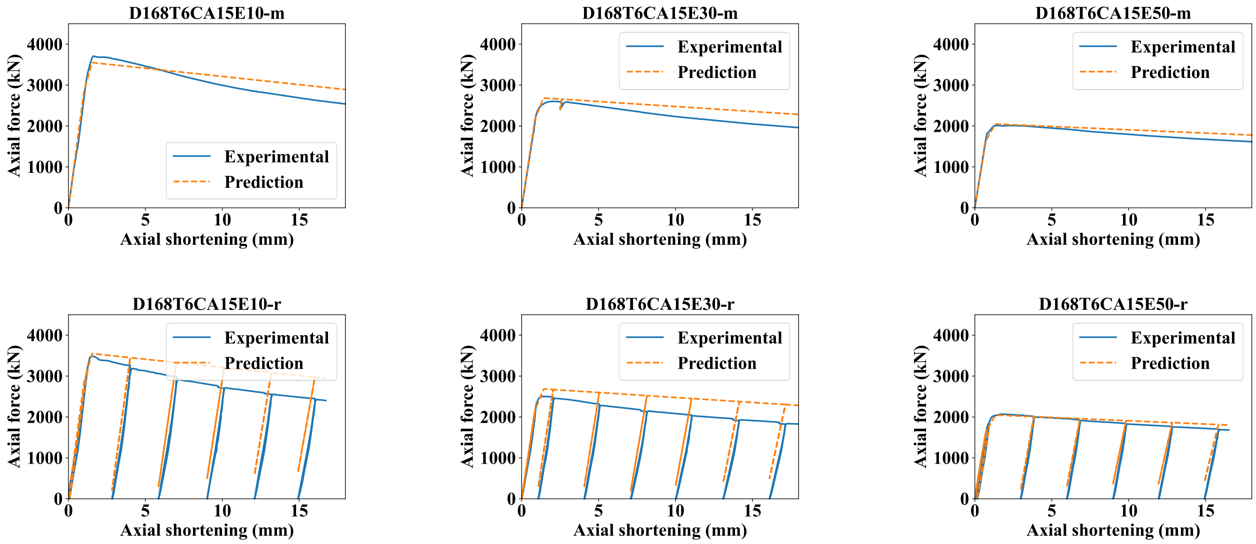

Fig.21. Prediction of proposed empirical model on validation set

Future investigations could focus on the eccentric compressive mechanical behavior of UHPCFST slender columns, with a particular emphasis on the stability aspects. Additionally, exploring the eccentric compressive mechanical behavior of UHPCFST with different cross-sectional shapes, such as rectangular, could also be a valuable research direction.

5. Conclusion

In the present work, 30 UHPCFST specimens are tested under monotonic and repeated eccentric compression to investigate the eccentric compressive mechanical performance of the UHPCFST. Based on the results and discussions presented in this paper, the following conclusions can be drawn.

1) The typical failure mode comprises three features: bulging of the steel tube, compressive crushing, and tensile cracking of the UHPC infill. The bulging of the steel tube is more likely to occur in specimens with smaller loading eccentricity, thinner tube thicknesses and higher UHPC coarse aggregate volume fraction. Specimens with larger loading eccentricity, thinner steel tube and higher UHPC coarse aggregate volume fraction tend to exhibit more severe compressive crushing and tensile cracking in the UHPC infill.

2) Stiffness degradation is observed, where the stiffness decreases with the increase of axial shortening. Specimens with thinner steel tube thickness, more coarse aggregates and larger eccentricity present a more serious stiffness degradation.

3) A new N-M curve for UHPCFST is proposed. The experimental results are used to evaluate the N-M curves of Yu, Han, EC4, AISC360, and proposed model, as well as their eccentric bearing capacities (also GB50936). The evaluation shows that the proposed model can provide accurate predictions on eccentric bearing capacity.

4) A formula for predicting eccentric compressive stiffness is derived with a parabolic shape function. Validated by experimental and numerical data, the propose model can give an acceptable prediction.

5) An empirical model is proposed to describe the force-axial shortening curve of UHPCFST under eccentric compression. The proposed model can give accurate force-axial shortening for UHPCFST under eccentric compression. This model can be applied in practical design, analysis, and numerical calculations of UHPCFST.

Acknowledgements

This work was supported by the National Natural Science Foundation of China (Grant Nos. 52178157, 51738011). The last author is grateful to the Royal Society for supporting the research collaboration (IEC\NSFC\181449).

Reference

[1] Scope C, Vogel M, Guenther E. Greener, cheaper, or more sustainable: Reviewing sustainability assessments of maintenance strategies of concrete structures. Sustainable Production and Consumption 2021;26:838–58.

[2] Baghban Golpasand G, Farzam M. Triaxial behavior of concrete containing recycled fibers- an experimental study. Construction and Building Materials 2023;406:133430.

[3] Jackson MD, Logan JM, Scheetz BE, Deocampo DM, Cawood CG, Marra F, et al. Assessment of material characteristics of ancient concretes, Grande Aula, Markets of Trajan, Rome. Journal of Archaeological Science 2009;36:2481–92.

[4] Jiao R-H, Feng D-C, Shen L, Wu G. A confined concrete model considering strain gradient effect of CFST column under eccentric load. Structures 2023;58:105645.

[5] Alatshan F, Osman SA, Hamid R, Mashiri F. Stiffened concrete-filled steel tubes: A systematic review. Thin-Walled Structures 2020;148:106590.

[6] Zheng J, Wang J. Concrete-Filled Steel Tube Arch Bridges in China. Engineering 2018;4:143–55.

[7] Han L. Concrete filled steel tubular structures-theory and practice. Science, Beijing; 2007.

[8] Chen Z, Gao F, Hu J, Liang H, Huang S. Creep and shrinkage monitoring and modelling of CFST columns in a super high-rise under-construction building. Journal of Building Engineering 2023;76:107282.

[9] Gu C, Wang X, Zhou X, Li X, Liao Y, Zheng N. Seismic behavior of prefabricated thin-walled CFST double-column bridge piers. Thin-Walled Structures 2024;198:111654.

[10] Chen D, Wu J, Zha X, Hou X. Study on selection of concrete-filled steel tubular X-column in large-scale cooling tower. Jianzhu Jiegou Xuebao/Journal of Building Structures 2021;42:322–31.

[11] Richard P, Cheyrezy MH. Reactive powder concretes with high ductility and 200-800 mpa compressive strength. vol. SP-144, 1994, p. 507–18.

[12] Su Y, Wu C, Li J, Li Z-X, Li W. Development of novel ultra-high performance concrete: From material to structure. Construction and Building Materials 2017;135:517–28.

[13] Yoo D-Y, Banthia N. Mechanical properties of ultra-high-performance fiber-reinforced concrete: A review. Cement and Concrete Composites 2016;73:267–80.

[14] Wu F, Xu L, Chi Y, Zeng Y, Deng F, Chen Q. Compressive and flexural properties of ultra-high performance fiber-reinforced cementitious composite: The effect of coarse aggregate. Composite Structures 2020;236:111810.

[15] Yan Y, Xu L, Li B, Chi Y, Yu M, Zhou K, et al. Axial behavior of ultra-high performance concrete (UHPC) filled stocky steel tubes with square sections. Journal of Constructional Steel Research 2019;158:417–28.

[16] Cai H, Lu D, Cheng T, Xu L. Circular steel tube-confined ultra-high performance concrete beam-column: Database, modeling, and design. Engineering Structures 2024;302:117376.

[17] Xu L, Lu Q, Chi Y, Yang Y, Yu M, Yan Y. Axial compressive performance of UHPC filled steel tube stub columns containing steel-polypropylene hybrid fiber. Construction and Building Materials 2019;204:754–67.

[18] Chen D, Zha X, Xu P, Li W. Stability of slender concrete-filled steel tubular X-column under axial compression. Journal of Constructional Steel Research 2021;185.

[19] Jani K, Patel PV. Analysis and design of diagrid structural system for high rise steel buildings. Procedia Engineering, vol. 51, 2013, p. 92–100.

[20] Chen D, Zha X, Hou X, Zhou G, Li G. Compression behavior of the concrete-filled steel tubular X-column. Jianzhu Jiegou Xuebao/Journal of Building Structures 2021;42:351–60.

[21] Shi Q, Cai W, Wang B. Axial Cyclic Testing of Concrete-Filled Steel Tube Columns in Diagrid Structures. Advances in Civil Engineering 2019;2019.

[22] Boake TM. Diagrid Structures: Systems, Connections, Details. Walter de Gruyter; 2014.

[23] Zhang Z, Guo X, Song Y, Sun Q, Tian P, Hu G. Numerical investigation and design of CFST columns strengthened by CFRP grid-reinforced ECC under eccentric compression. Engineering Structures 2024;301:117253.

[24] Zhou J, Chen Z, Liu D, Qin W, Li J. Experimental and numerical investigations on eccentric compression behavior of square CFST columns with inner spiral stirrup. Structures 2023;57:105196.

[25] Zheng Y, Liang W, Ma S, Zeng S. Behavior of stiffened and multi-cell L-shaped CFST columns under eccentric compression. Thin-Walled Structures 2022;174:109156.

[26] Zheng Y, Lin Y, Liang W. Concentric and eccentric compressive behaviors of stiffened T-shaped CFST columns. Journal of Constructional Steel Research 2024;212:108229.

[27] Ke X, Wei H, Yang L, Sun H. Analysis and calculation method for concrete-encased CFST columns under eccentric compression. Journal of Constructional Steel Research 2023;206:107927.

[28] Fanghong W, Xu L, Yu M. Experimental investigation of axially loaded circular ultra-high performance concrete with coarse aggregate (CA-UHPC) filled steel tube slender columns. Structures 2023;58:105355. https://doi.org/10.1016/j.istruc.2023.105355.

[29] Lu Q, Xu L, Chi Y, Deng F, Yu M, Hu X. A novel analysis-oriented theoretical model for steel tube confined ultra-high performance concrete. Composite Structures 2021;264:113713. https://doi.org/10.1016/j.compstruct.2021.113713.

[30] Wu F, Zeng Y, Li B, Lyu X. Experimental Investigation of Flexural Behavior of Ultra-High-Performance Concrete with Coarse Aggregate-Filled Steel Tubes. Materials 2021;14:6354. https://doi.org/10.3390/ma14216354.

[31] GB/T 228.1:2010: Metallic materials -Tensile testing - Part 1: Method of test at room temperature. 2010.

[32] T/CCPA 35—2022/ T/CBMF 185—2022: Specification for design of ultra-high performance concrete structures. 2022.

[33] Yu M, Xu H, Ye J, Chi Y. A unified interaction equation for strength and global stability of solid and hollow concrete-filled steel tube columns under room and elevated temperatures. Journal of Constructional Steel Research 2018;148:304–13.

[34] ANSI/AISC 360-16: Specification for Structural Steel Buildings 2016.

[35] Eurocode 4: Design of composite steel and concrete structures Part 1-1: General rules and rules for buildings 1994.

[36] CN-GB50936-2014: Technical code for concrete-filled steel tubular structures (press in Chinese) 2014.

[37] Zha X, Yu M, Zhong S. Consistency study on bearing capacity formulae in the Chinese Code for design of concrete filled steel tubular structures. Journal of Building Structures 2013;34:11–20.

[38] Yu C, Yu M, Xu L, Liu S, Wang T, Ye J. Experimental research on mechanical behavior of UHPCFST under repeated axial compression. Journal of Constructional Steel Research 2024;218:108690.

[39] Yu C, Yu M, Xu L, Yang Y, Ye J. Experimental investigation of the behavior of UHPCFST under repeated axial tension. Engineering Structures 2024;314:118293. https://doi.org/10.1016/j.engstruct.2024.118293.

[40] Chung K, Park S, Choi S. Fire resistance of concrete filled square steel tube columns subjected to eccentric axial load. Int J Steel Struct 2009;9:69–76.

[41] Yu M, Zha, X. A UNIFIED FIBER ELEMENT MODEL FOR SOLID AND HOLLOW CONCRETE-FILLED STEEL TUBE. Industrial Construction 2014;44:123-129+107.